analytical chemistry

pubs.acs.org/ac Article

Fluorescence Biosensor for One-Step Simultaneous Detection of *Mycobacterium tuberculosis* Multidrug-Resistant Genes Using nanoCoTPyP and Double Quantum Dots

Ou Hu, Zeyu Li, Qidi He, Yanli Tong,* Yaoju Tan,* and Zuanguang Chen*

Cite This: *Anal. Chem.* 2022, 94, 7918−7927 Read Online

ACCESS | Metrics & More | Article Recommendations | Supporting Information

ABSTRACT: The diagnosis of multidrug-resistant tuberculosis (MDR-TB) is crucial for the subsequent drug guidance to improve therapy and control the spread of this infectious disease. Herein, we developed a novel florescence biosensor for simultaneous detection of *Mycobacterium tuberculosis* (Mtb) multidrug-resistant genes (rpoB531 for rifampicin and katG315 for isoniazid) by using our synthesized nanocobalt 5,10,15,20-tetra(4-pyridyl)-21*H*,23*H*-porphine (nanoCoTPyP) and double quantum dots (QDs). Several nanoCoTPyPs with different charges and morphology were successfully prepared via the surfactant-assisted method and their quenching ability and restoring efficiency for DNA detection were systematically analyzed. It was found that spherical nanoCoTPyP with positive charge exhibited excellent quenching effect and sensing performance for the two DNAs' detection due to its affinity differences towards single-stranded DNA (ssDNA) and double-stranded DNA (dsDNA). ssDNA attached on QDs (QDs-ssDNA) was specifically hybridized with targets to form QDs-dsDNA, resulting in fluorescence recovery due to the disruption of the interactions between nanoCoTPyP and ssDNA. Two drug-resistant genes could be simultaneously quantified in a single run and relatively low limits of detection (LODs) were obtained (24 pM for T1 and 20 pM for T2). Furthermore, the accuracy and reliability of our method were verified by testing clinical samples. This simple and low-cost approach had great potential to be applied in clinical diagnosis of MDR-TB.

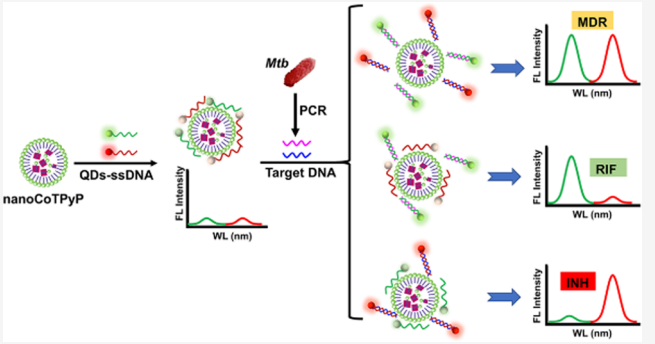

INTRODUCTION

Mycobacterium tuberculosis (Mtb), the pathogen of tuberculosis (TB), remains the deadliest bacterial pathogen in the world.[1] Moreover, the emergency of multidrug-resistant tuberculosis (MDR-TB) has aggravated the prevalence of TB. Rifampicin (RIF) and isoniazid (INH) are the two most potent frontline anti-TB drugs, and the resistance to at least one drug is regarded as MDR-TB.[2,3] Furthermore, resistance to RIF and INH determines the effectiveness of the recommended therapeutic schedule.[4] The failure of resistance diagnosis will not only make the patients suffer from pain, but also cause the disease to spread to healthy people. The current identification methods of MDR-TB mainly include drugs susceptibility test (DST) and Xpert MTB/RIF (Xpert) assay.[5,6] Although DST and Xpert methods are both sensitive to detect resistance, DST is time-consuming, with a period of 4−14 days, and Xpert assay is mainly designed for the detection of Mtb and RIF resistance.[7,8] Therefore, to achieve the ultimate goal of a TB-free world by 2035, it is still necessary to develop rapid, economical, and sensitive methods for the diagnosis of MDR-TB, especially resistance to RIF and INH.

Recently, several nanomaterial-based biosensor methods have been developed for the detection of Mtb multidrug-resistant genes. For example, Chan and his colleagues[9] successfully employed oligonucleotide-functionalized CdSe/CdS and $CdSe_{1-x}S_x$/CdS nanorods to simultaneous detect multiplexed genes of Mtb based on the solid-phase polymerase chain reaction (SP-PCR). But the operation of this strategy was more complicated than that of the traditional polymerase chain reaction (PCR), leading to a longer analysis time (2.5 h). A highly sensitive fluorescence biosensor based on the graphdiyne nanosheet and organic fluorophores was utilized for identification of Mtb drug-resistant mutants with a low limit of detection of 25 pM.[10] However, this approach could not simultaneously quantify multiple DNAs due to the different excitation spectra of organic fluorophores. Therefore, there are still many challenges and more efforts should be made to simultaneously detect Mtb multidrug-resistant genes.

Received: February 13, 2022
Accepted: May 10, 2022
Published: May 20, 2022

https://doi.org/10.1021/acs.analchem.2c00723
Anal. Chem. 2022, 94, 7918−7927

Scheme 1. Schematic Illustration of Fluorescent Biosensing for One-Step Simultaneous Detection of Multidrug-Resistant Genes Based on Double QDs-ssDNA and nanoCoTPyP

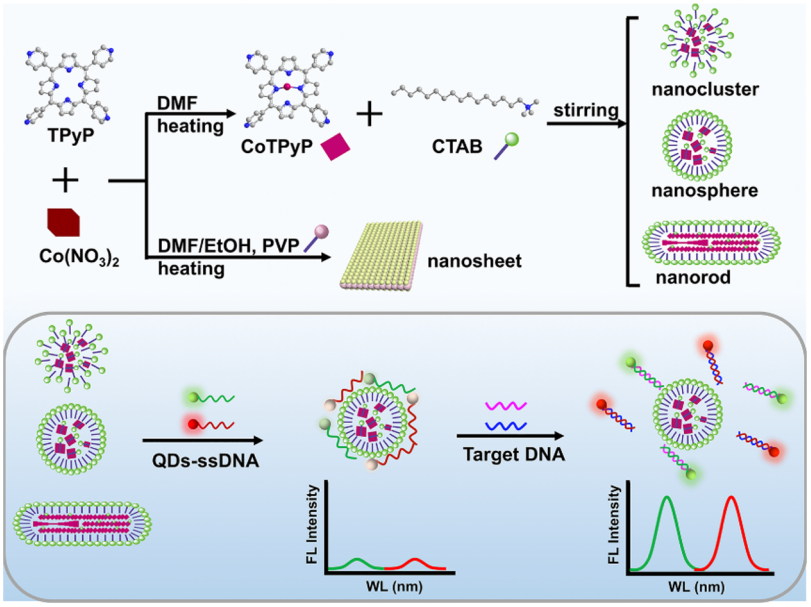

A nanomaterial-based fluorescence biosensor with the advantages of simple operation and high sensitivity has been widely used to detect multiplexed targets, especially the quantum dots (QDs)-based fluorescence biosensor.[11−14] Compared with traditional organic fluorophores, QDs have unique optical properties, including strong photostability, a broad excitation spectrum, and a narrow emission spectrum.[15,16] More importantly, QDs have the advantages of single excitation and multiple emission, contributing to their being ideal fluorescence probes for simultaneous detection of multiple targets.[17] Metal organic frameworks (MOFs) consisting of an organic linker and inorganic metal have drawn considerable attraction in the field of biosensing due to their outstanding characteristics, including a great fluorescence quenching ability, a large specific surface area, structural diversity, easy functionalization, etc.[18−21] Combinations of MOF materials such as MIL-101,[22] UiO-66-NH_3,[23] CS-ZIF-8-La,[24] Fe_3O_4@MIL-100,[25] and lanthanum-based MOFs[26] and organic fluorophores have been successfully utilized as sensing platforms for nucleic acid detection. Metalloporphyrin and its derivatives with a large π-conjugated aromatic structure, as a kind of MOFs, have shown unique features in terms of catalysis, fluorescence quenching ability, and assembly.[27,28] Furthermore, metalloporphyrin-based nanomaterials with different morphologies and charges can be easily and controllably synthesized by the surfactant-assisted method.[29] It has been reported that the sensing performance of MOFs can be affected by many factors, including their geometry structure, surface charge properties, size, etc.[30] To further explore the properties of metalloporphyrins and expand their applications, we herein synthesized nanocobalt 5,10,15,20-tetra(4-pyridyl)-21*H*,23*H*-porphine (nanoCoTPyP) with different geometry structures and charges to systematically analyze its sensing performance.

Herein, we developed a novel, one-step, and low-cost fluorescence sensing method for simultaneous detection of Mtb multidrug-resistant genes (rpoB gene at 531 position and katG gene at 315 position) based on nanoCoTPyP and double QDs. The most frequent mutations for resistance to RIF and INH occur at codon 531 of rpoB gene (TCG to TTG) and codon 315 of katG gene (AGC to ACC), respectively.[6,31] Therefore, two gene fragments containing the two mutations were selected as targets (named as T1 and T2). The principle of detection mechanism is illustrated in Scheme 1. First, four different structures of nanoCoTPyP were synthesized. QDs1 (green color) and QDs2 (red color) were, respectively, attached with ssDNA1 and ssDNA2, then mixed to construct the double QDs-ssDNA probes. The two fluorescence emission peaks of the double QDs-ssDNA were located at 535 and 648 nm (Figure S1A). The double QDs-ssDNA could adsorb onto nanoCoTPyP via electrostatic interaction, $\pi-\pi$ stacking, and hydrogen bonding,[22,32] leading to fluorescence quenching due to the fluorescence resonance energy transfer (FRET) and photoinduced electron transfer (PET).[30,33,34] As shown in Figure S1B, the UV−vis absorption spectra of nanoCoTPyP overlapped with the fluorescence emission spectrum of the double QDs-ssDNA, which was beneficial for the FRET processes. However, in the presence of target DNAs, target DNAs and ssDNA hybridized specifically to form more stable double-stranded DNA (dsDNA). The rigidity of the double-chain structure decreased the affinity, resulting in the detachment of double QDs-dsDNA and fluorescence restoring. This fluorescence biosensor could simultaneously quantify two drug-resistant genes in a single run due to the two emission peaks of double QDs (T1 vs ssDNA1; T2 vs ssDNA2). More importantly, we explored in detail the effects of MOFs' geometry structure and charge on the sensing performance by using three-dimensional (3D) and two-dimensional (2D) nanoCoTPyP. This simple and economical approach could accurately recognize a single-base mismatched nucleotide sequence, and we verified the practicability using clinical MDR-TB strains.

EXPERIMENTAL SECTION

Preparation of nanoCoTPyP-1, nanoCoTPyP-2, and nanoCoTPyP-3. The preparation processes are illustrated in the upper part of Scheme 1. Firstly, metalation of 5,10,15,20-

https://doi.org/10.1021/acs.analchem.2c00723
Anal. Chem. 2022, 94, 7918−7927

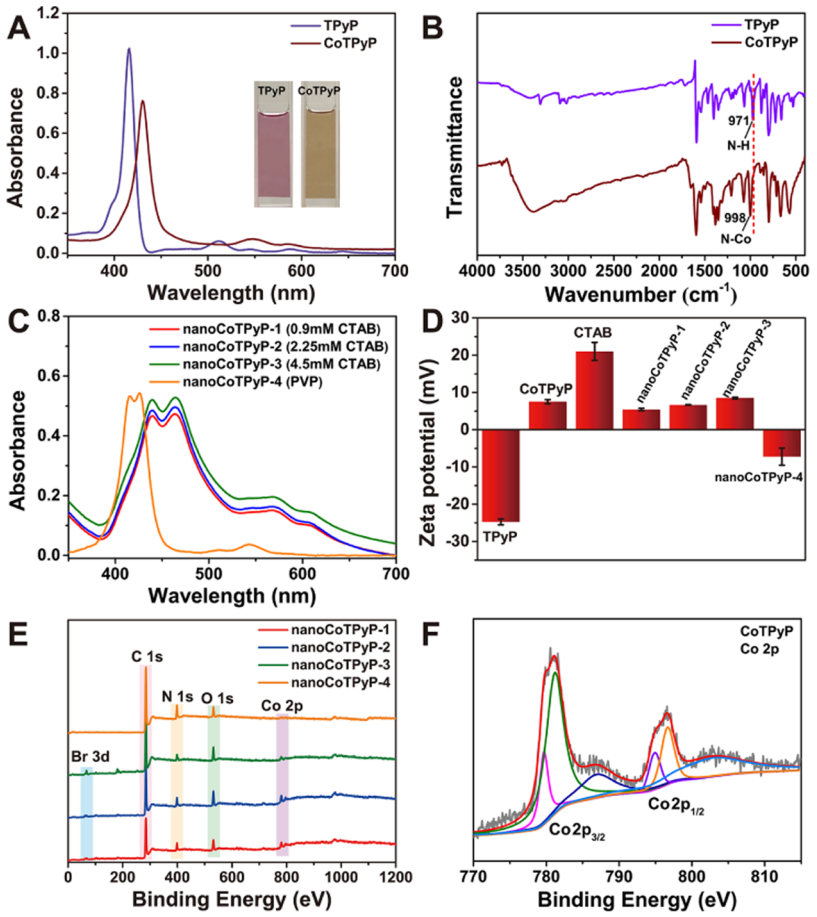

Figure 1. (A) UV−vis absorption spectra of TPyP and CoTPyP. Inset: photograph of TPyP and CoTPyP DMF solution under visible light; (B) FTIR spectra of TPyP and CoTPyP; (C) UV−vis absorption spectra of nanoCoTPyP; (D) ζ-potential of TPyP, CoTPyP, CTAB, and nanoCoTPyP; (E) XPS spectra of nanoCoTPyP; (F) high-resolution XPS spectra of Co 2p for CoTPyP.

tetra(4-pyridyl)-21*H*,23*H*-porphine (TPyP) was carried out to obtain cobalt 5,10,15,20-tetra(4-pyridyl)-21*H*,23*H*-porphine (CoTPyP). Accordingly, 0.0618 g of TPyP (0.1 mmol) dissolved in 30 mL of dimethylformamide (DMF) was heated at 150 °C for 10 min, and then 0.1164 g of $Co(NO_3)_2{\cdot}6H_2O$ (0.4 mmol) was added. The mixture was refluxed at 150 °C for 5 h. Thereafter, the chilled water was slowly added into the reaction, and the brown CoTPyP product was collected by vacuum filtration after standing at room temperature for 2 h. NanoCoTPyP-1, nanoCoTPyP-2, and nanoCoTPyP-3 were synthesized by surfactant-assisted self-assembly method, where the cationic surfactant hexadecyl trimethyl ammonium bromide (CTAB) was used. Briefly, 600 μL of CoTPyP DMF solution (2×10^{-4} M) was added into 15 mL of CTAB aqueous solution. The mixture was stirred vigorously at room temperature for 20 min, and a transparent yellowish solution was obtained without purification processes. Three different concentrations of CTAB aqueous solution (0.9, 2.25, and 4.5 mM) were designed for nanoCoTPyP-1, nanoCoTPyP-2, and nanoCoTPyP-3, respectively. The concentrations of CoTPyP were determined by using the extinction coefficients (λ_{max} = 430 nm, ε = 62,300 M^{-1} cm^{-1}).[35]

Preparation of nanoCoTPyP-4. The synthesis procedures are shown in the upper part of Scheme 1. NanoCoTPyP-4 was synthesized by the surfactant-assisted synthetic method, where the surfactant poly(vinylpyrrolidone) (PVP) was utilized. Briefly, 8.8 mg of $Co(NO_3)_2{\cdot}6H_2O$ (0.03 mmol) and 40 mg of PVP were dissolved in 24 mL of a DMF/ethanol (3:1) mixture. Eight milliliters of a DMF/ethanol (3:1) mixture containing 0.0062 g of TPyP (0.01mmol) was added dropwise into the above mixture; then, the solution was sonicated for 10 min. Afterwards, the mixture was heated at 80 °C for 24 h. Finally, the dark purple product was washed twice with ethanol, collected by centrifuging at 8000 rpm for 10 min, and dried in a vacuum.

Preparation of nanoCoTPyP-5 and nanoCoTPyP-6. NanoCoTPyP-5 and nanoCoTPyP-6 were synthesized by a similar procedure as for nanoCoTPyP-1, except for the use of a surfactant. The anionic surfactant sodium dodecyl sulfate (SDS) was utilized to prepare nanoCoTPyP-5 (8 mM SDS) and nanoCoTPyP-6 (10 mM SDS).

Preparation of Double QDs and Double QDs-ssDNA. The double QDs and double QDs-ssDNA were prepared according to the protocol of our previous work.[36] The detailed procedures are provided in the Supporting Information.

Simultaneous Detection of Multiple DNA. Ten microliters of nanoCoTPyP-2 (4.0 μM) was added into 20 μL of QDs1-ssDNA1 (3.0 μM) and 20 μL of QDs2-ssDNA2 (0.5 μM). The mixture was followed by 4 min incubation under room temperature. Afterwards, the as-prepared mixture was incubated with T1 (10 μL) and T2 (10 μL) at different concentrations under room temperature for 7 min. For monitoring the hybridization process, a single excitation wavelength of 380 nm was employed to record the

https://doi.org/10.1021/acs.analchem.2c00723
Anal. Chem. 2022, 94, 7918−7927

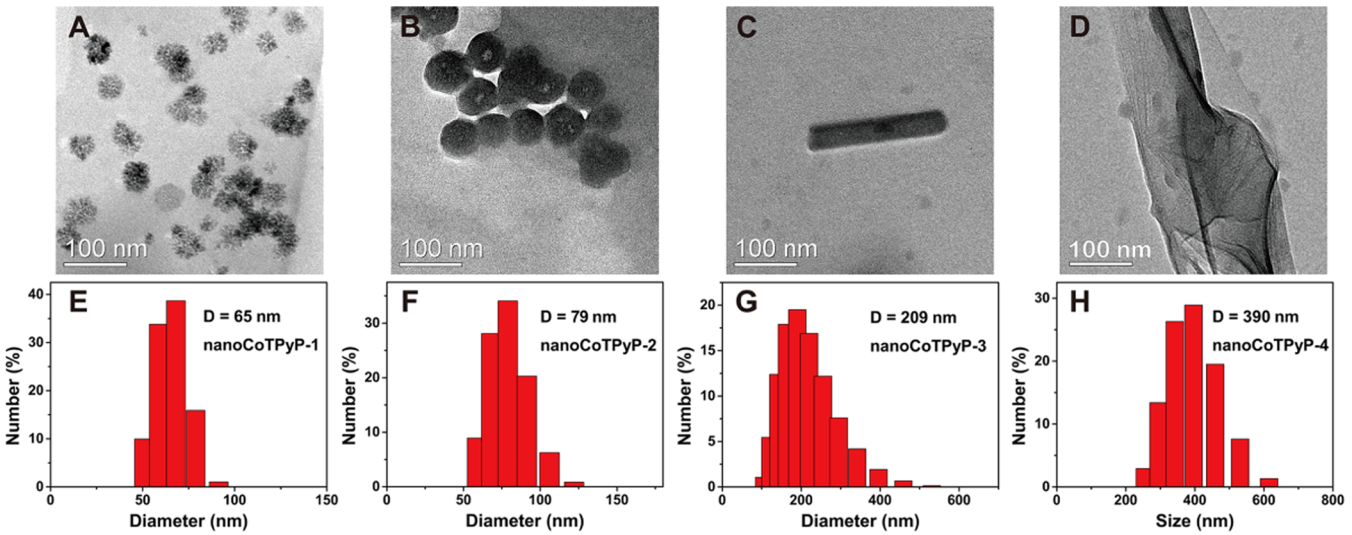

Figure 2. Characterization of nanoCoTPyP. The TEM images of nanoCoTPyP-1 (A), nanoCoTPyP-2 (B), nanoCoTPyP-3 (C), and nanoCoTPyP-4 (D). The DLS distribution of nanoCoTPyP-1 (E), nanoCoTPyP-2 (F), nanoCoTPyP-3 (G), and nanoCoTPyP-4 (H).

fluorescence emission spectra of the mixture. Two emission spectra were utilized to determine T1 (λ_{em} = 535 nm) and T2 (λ_{em} = 648 nm), respectively. The nucleotide sequences of the DNA used in this study are listed in Table S1.

Fluorescence Response of PCR Samples for Clinical MDR Strains. Five clinical MDR-TB strains, three clinical RIF-resistant strains, five clinical INH-resistant strains, and seven nonresistant strains were kindly provided by Guangzhou Chest Hospital (Guangzhou, China). All strains were treated with the Ezup column yeast genomic DNA purification kit (Sangon Biotechnology Co. Ltd., Shanghai, China) for genomic DNA extraction. The DNAs were amplified by PCR with two pairs of primers to obtain the RIF-resistant gene fragments (314 bp) and INH-resistant gene fragments (232 bp). The PCR products were commercially sequenced to confirm the mutation sites (Table S2). Prior to the fluorescence spectra measurement, the PCR products were heated at 100 °C for 7 min and immediately placed on ice for 5 min to obtain ssDNA. The measurement procedures were the same as above.

RESULTS AND DISCUSSION

Characterization of nanoCoTPyP. The UV−vis absorption spectra of TPyP and CoTPyP are shown in Figure 1A. TPyP exhibited a Soret band at 416 nm and four Q bands at 512, 546, 587, and 644 nm. However, after the formation of CoTPyP, the Soret band showed a red shift of 14 nm and the four Q bands reduced to two Q bands. The occurrence of this phenomenon possibly resulted from the perturbation of the π electron transition and the degeneration of electronic transitions in the Q band region owing to the insertion of cobalt(II).[37] The color of their DMF solution obviously changed from purple into brown (inset of Figure 1A). Additionally, the Fourier transform infrared (FTIR) spectra in Figure 1B revealed that the C−N bending vibration at 971 cm^{-1} of TPyP shifted to the N−Co bending vibration at 998 cm^{-1}. The X-ray photoelectron spectroscopy (XPS) analysis confirmed the appearance of Co in the XPS spectrum of CoTPyP compared with that of TPyP (Figure S2A). All of the results suggested the successful preparation of CoTPyP. The UV−vis absorption spectra of the four nanoCoTPyP in Figure 1C illustrated the Soret bands and two Q bands. It is worth noting that their Soret bands were split into two absorption peaks, indicating the formation of J-type aggregates.[29,38] ζ-Potential analysis was further performed for the study of surface potential. As seen from Figure 1D, TPyP was negatively charged, whereas the opposite ζ-potential was found in CoTPyP after the insertion of cobalt(II). The cationic surfactant CTAB was positively charged. With the increase of cationic surfactant CTAB for self-assembly, the gradually increasing positive potentials were found by nanoCoTPyP-1 (+5.42 mV), nanoCoTPyP-2 (+6.65 mV), and nanoCoTPyP-3 (+8.47 mV). However, nanoCoTPyP-4 was negatively charged (−7.23 mV). Moreover, XPS measurement was applied to investigate the chemical composition of nanoCoTPyP and valence state of cobalt. From Figure 1E, the elements of these four nanoCoTPyPs were primarily composed of C, N, O, and Co, similar to CoTPyP (Figure S2A), but nanoCoTPyP-1, nanoCoTPyP-2, and nanoCoTPyP-3 additionally contained Br due to the usage of CTAB. High-resolution XPS (Co 2p) analyses were also conducted for CoTPyP and nanoCoTPyP-4 (Figures 1F and S2B). As displayed in Figure 1F, Co 2p of CoTPyP had two main peaks for Co $2p_{3/2}$ and Co $2p_{1/2}$ centered on ∼780.98 and ∼796.58 eV. The two fitted peaks for Co $2p_{3/2}$ occurred at 779.67 and 781.17 eV, and dual doublets for Co $2p_{1/2}$ presented at 793.90 and 796.66 eV. The two broad peaks at 786.89 and 802.75 eV were assigned to the satellite peaks. These results were completely consistent with the valence state of cobalt metal of 2^+.[39] As for nanoCoTPyP-4, the XPS of Co 2p was similar to that of CoTPyP, again indicating the valence state of cobalt metal as 2^+ (Figure S2B). Therefore, cobalt(II) was demonstrated to exist in nanoCoTPyP-1, nanoCoTPyP-2, nanoCoTPyP-3, and nanoCoTPyP-4.

The morphology and size of nanoCoTPyP-1, nanoCoTPyP-2, nanoCoTPyP-3, and nanoCoTPyP-4 were further investigated by transmission electron microscopy (TEM) and dynamic light scattering (DLS) measurements. As depicted in Figure 2, the TEM images of these four nanoCoTPyPs exhibited different architectures. NanoCoTPyP-1 presented as nanoclusters with an average size of 65 nm; nanoCoTPyP-2 showed a spherical structure with a size of almost 79 nm;

https://doi.org/10.1021/acs.analchem.2c00723
Anal. Chem. 2022, 94, 7918−7927

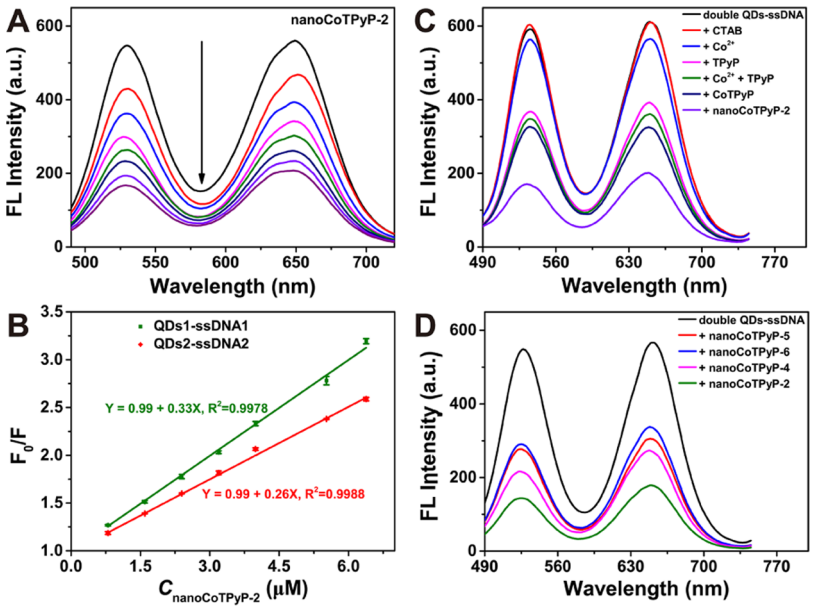

Figure 3. (A) Fluorescence quenching of double QDs-ssDNA with addition of different concentrations of nanoCoTPyP-2 (0.8−6.4 μM); (B) Stern−Volmer plots of double QDs-ssDNA being quenched by nanoCoTPyP-2; (C) fluorescence quenching ability of CTAB (2.25 mM), Co^{2+} (6.4 μM), TPyP (6.4 μM), Co^{2+}+TPyP (6.4 μM), CoTPyP (6.4 μM), and nanoCoTPyP-2 (6.4 μM) toward double QDs-ssDNA; (D) comparison of the fluorescence quenching ability between different surfactant-assisted synthesized nanoCoTPyPs.

nanoCoTPyP-3 existed as nanorods with an average size of 209 nm, and nanoCoTPyP-4 was shown to have a sheet structure with an average size of 390 nm. It was found that three different nanostructures were successfully synthesized by controlling the concentration of CTAB. Previous work has reported that the critical micelle concentration (CMC) of CTAB was 0.9∼0.92 mM.[40] When 0.9 mM CTAB was used, micellization began to occur, and nanoclusters were inclined to be obtained due to the slight deficiency of CTAB. As the CTAB concentration increased to 2.25 mM, CoTPyP molecules regularly aggregated into nanospheres. On account of the higher CTAB concentration, a larger-sized structure of nanorods tended to be formed. Therefore, the different aggregations of CoTPyP molecules were highly affected by the concentration of the surfactant, which was also found by other researchers.[41] It was reported that surfactant PVP could be applied to control the growth of nanocrystals for the preparation of ultrathin nanosheets.[32] The atomic force microscopy (AFM) analysis of nanoCoTPyP-4 confirmed that the thickness of nanoCoTPyP-4 was about 2 nm (Figure S2C,D), showing that it consisted of ultrathin two-dimensional nanosheets.

Characterization of Double QDs and Double QDs-ssDNA. MPA-capped double CdTe QDs were selected as the fluorescence probes due to their excellent properties, simple synthesis method, and previous successful application for multiple targets.[36] The DLS diameters of QDs1 and QDs2 were 2.1 and 4.6 nm (Figure S3), and fluorescence quantum yields of QDs1 and QDs2 were 57.46 and 70.27%. The optical properties of QDs and QDs-ssDNA are shown in Figure S4. QDs1 with green color displayed a UV−vis absorbance peak at 493 nm, and the fluorescence emission peak of QDs1 was located at 542 nm (λ_{ex} = 380 nm). QDs2 with red color exhibited the UV−vis absorbance peak at 597 nm and a fluorescence emission peak at 630 nm (λ_{ex} = 380 nm). QDs were modified with ssDNA to prepare QDs-ssDNA by the formation of amide covalent bonds. The UV−vis absorption spectra of QDs1-ssDNA1 and QDs2-ssDNA2 showed a new absorption peak at 260 nm, indicating the successful preparation of QDs-ssDNA (Figure S4A,B). Furthermore, the fluorescence emission spectra had a 7 nm blue shift for QDs1-ssDNA1 and an 18 nm red shift for QDs2-ssDNA2, further verifying the functionalization of ssDNA (Figure S4C,D). Double QDs-ssDNA also showed the blue and red shifts of these two emission peaks (Figure S1A). Since the two maximum emission peaks of the double QDs-ssDNA were different and non-interfering, double QDs-ssDNAs were suitable for simultaneous determination of multiple targets (λ_{em} = 535 nm for T1, λ_{em} = 648 nm for T2). Furthermore, the numbers of ssDNA per QD were determined to be 1.1 (ssDNA1) and 1.3 (ssDNA2) using UV absorption spectra (Figure S5), suggesting that there was about one strand of DNA per QD.

Fluorescence Quenching Abilities of NanoCoTPyP toward Double QDs-ssDNA. The fluorescence quenching abilities of nanoCoTPyP play an important role in the subsequent DNA sensing. Therefore, the fluorescence emission spectra of double QDs-ssDNA were collected after the addition of four nanoCoTPyPs (nanoCoTPyP-1∼nanoCoTPyP-4). As shown in Figures 3A and S6, with the increase in concentrations of nanoCoTPyP, the intensities of the two emission peaks decreased gradually, and no significant wavelength shifts were observed in the maximum emission peaks. To study the relationships between fluorescence intensity and nanoCoTPyP concentration, Stern−Volmer plots were drawn to quantify the fluorescence quenching of double QDs-ssDNA by the four nanoCoTPyPs according to the Stern−Volmer equation $F_0/F = 1 + K_{sv}[Q]$. In this equation, F_0 and F are the fluorescence intensities of double QDs-ssDNA in the absence and presence of nanoCoTPyP, respectively, [Q] is the concentration of nanoCoTPyP, and K_{sv} is the Stern−Volmer quenching constant. Quenching constant K_{sv} was used to estimate the quenching efficiency of nanoCoTPyP. In our work, K_{sv1} was applied for QDs1-

https://doi.org/10.1021/acs.analchem.2c00723
Anal. Chem. 2022, 94, 7918−7927

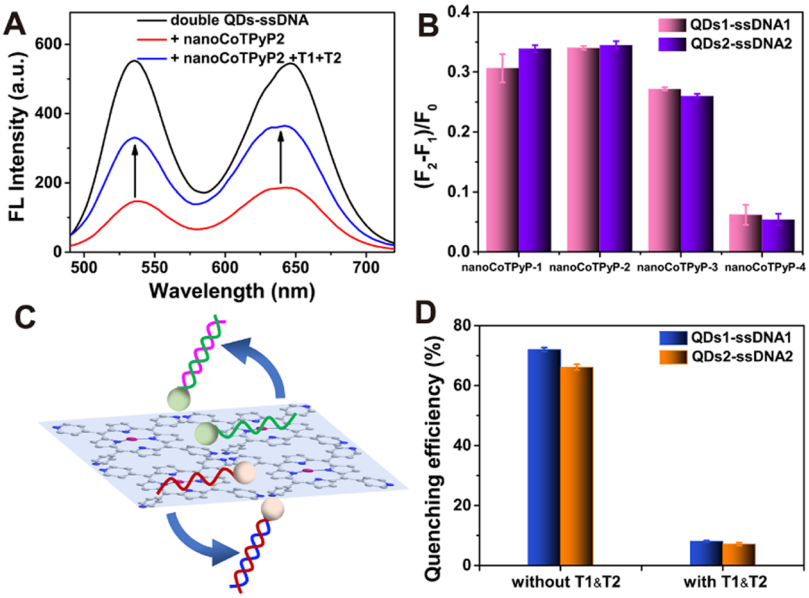

Figure 4. (A) Fluorescence restoration of double QDs-ssDNA with addition of T1 (20 nM) and T2 (20 nM); (B) fluorescence recovery ratios of different nanoCoTPyPs for DNA detection; (C) schematic illustration of the re-adsorption of double QDs-dsDNA on nanosheets; (D) fluorescence quenching efficiency of nanoCoTPyP-2 towards double QDs-ssDNA and double QDs-dsDNA.

ssDNA1 and K_{sv2} was applied for QDs2-ssDNA2. As seen from Figure 3B, the K_{sv1} and K_{sv2} of nanoCoTPyP-2 towards the fluorescence intensities of double QDs-ssDNA were 0.33×10^6 and 0.26×10^6 M^{-1}, respectively. The values of F_0/F were linearly related with the concentration of nanoCoTPyP-2 in the range of 0.8 μM-6.4 μM, with the square of correlation coefficient R^2 = 0.9978 and 0.9988. Similar linear relationships were observed as the concentrations of nanoCoTPyP-1, nanoCoTPyP-3, and nanoCoTPyP-4 increased from 0.8 to 6.4 μM, R^2 > 0.993 (Figure S6). The K_{sv1} and K_{sv2} of the four nanoCoTPyPs are summarized in Table S3. It can be seen that these four nanoCoTPyPs exhibited excellent quenching ability towards double QDs-ssDNA without obvious differences. In addition, the maximum quenching was observed for the 8.0 μM nanoCoTPyP-2 (Figure S7). It has been reported that ssDNA-labeled fluorophore probes could be attached on MOFs via various interactions, including electrostatic interaction, $\pi-\pi$ stacking, and hydrogen bonding, leading to fluorescence quenching because of FRET and PET processes.[22,32] Therefore, the positively charged nanoCoTPyP-1, nanoCoTPyP-2, and nanoCoTPyP-3 could adsorb negatively charged double QDs-ssDNA through electrostatic interaction, besides $\pi-\pi$ stacking and hydrogen bonding. As for the negatively charged nanoCoTPyP-4, the $\pi-\pi$ stacking and hydrogen bonding were the main interactions. This explained well why the quenching effect of 2D nanosheets with highly exposed surfaces was slightly worse than that of 3D nanoclusters, nanospheres, and nonorods. According to the literature,[42] nanomaterials with larger surface area were more beneficial for fluorescence quenching due to their more accessible active sites for energy/electron transfer. Compared with the nanoCoTPyP-1 nanocluster, spherical nanoCoTPyP-2 had a slightly smaller surface area, but it possessed more accessible active sites, thus showing slightly better quenching efficiency.

NanoCoTPyP-2 was further compared with Co^{2+}, TPyP, CoTPyP, and CTAB (Figures 3C and S8). It could be seen that CTAB aqueous solution could hardly quench the double QDs-ssDNA. The quenching efficiency of nanoCoTPyP-2 was over 70%, which was much higher than that of Co^{2+} (3%), TPyP (38%), the mixture of Co^{2+} and TPyP (41%), and CoTPyP (45%). These results implied that the excellent quenching features of nanoCoTPyP-2 primarily came from its entire 3D structures. Therefore, in our system, QDs acted as donors, while nanoCoTPyPs acted as acceptors (quenchers).

To better understand the effect of surface charge properties on the interactions, nanoCoTPyP-5 and nanoCoTPyP-6 with negative charges were synthesized using SDS. Considering that the CMC of SDS was 8 mM,[43] we synthesized nanoCoTPyP-5 and nanoCoTPyP-6 using 8 and 10 mM SDS, respectively. The UV−vis absorption spectra of nanoCoTPyP-5 and nanoCoTPyP-6 displayed a split Soret band, implying the J-type aggregates of CoTPyP molecules as well (Figure S9A). ζ-Potential measurements demonstrated that the use of surfactant could change the surface charge of the nanoCoTPyP (Figure S9B), suggesting that the self-assembled nanoCoTPyP might be enwrapped by the surfactant. The TEM images showed that nanoCoTPyP-5 and nanoCoTPyP-6 presented as nanospheres and nanorods, respectively (Figure S9C,D). The quenching abilities of nanoCoTPyP-5 and nanoCoTPyP-6 were further evaluated (Figure 3D). The results showed that nanoCoTPyP-2 with positive charge was superior to the negatively charged nanoCoTPyP-4, nanoCoTPyP-5, and nanoCoTPyP-6, confirming the significant influence of surface charge properties. Moreover, we found that when the charges of nanomaterials were the same, the plane structures (nanoCoTPyP-4) indeed enhanced the quenching ability compared with 3D structures (nanoCoTPyP-5 and nanoCoTPyP-6).

DNA Detection Performance of NanoCoTPyP. The feasibility of the four nanoCoTPyPs for simultaneous detection of rpoB531 gene (T1) and katG315 gene (T2) were further investigated and contrasted. The double QDs-ssDNAs were reacted with four nanoCoTPyP separately for 10 min, then 10 μL of T1 and 10 μL of T2 were added into the mixture and incubated for 30 min at room temperature. As displayed in

https://doi.org/10.1021/acs.analchem.2c00723
Anal. Chem. 2022, 94, 7918−7927

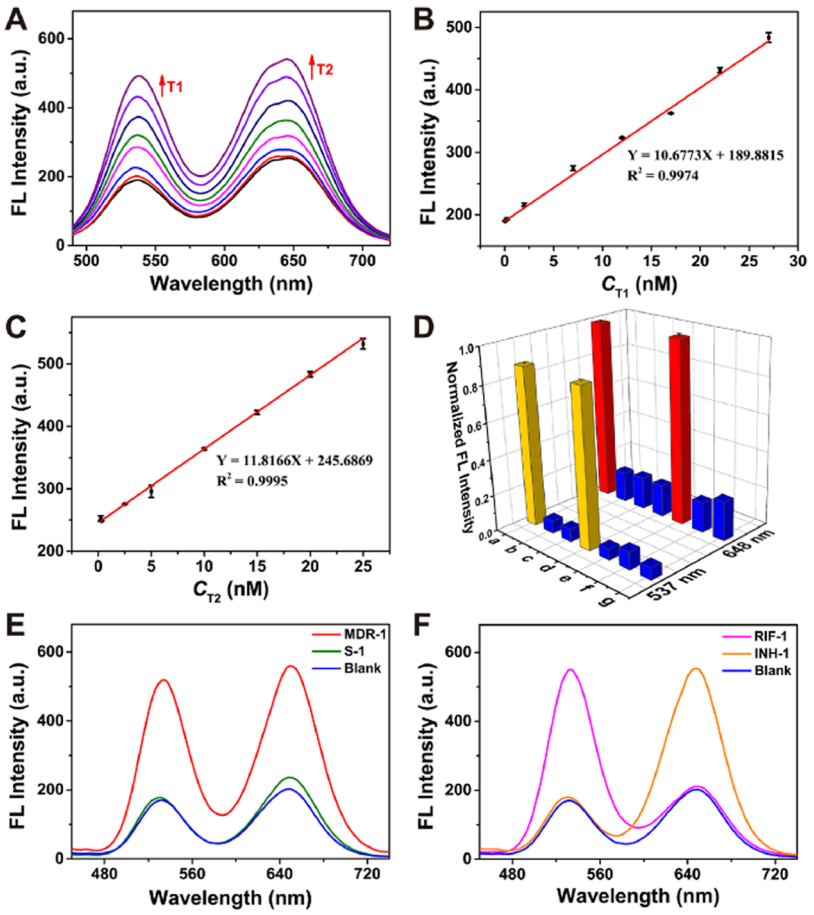

Figure 5. (A) Fluorescence emission spectra for simultaneous detection of T1 (0.04−27 nM) and T2 (0.03−25 nM) in the presence of CoTPyP-2 (4.0 μM); (B) linear relationships of fluorescence intensity at 535 nm versus concentrations of T1; (C) linear relationships of fluorescence intensity at 648 nm versus concentrations of T2; (D) selectivity study of this fluorescence biosensor (a: T1/T2 mixture; b: blank; c: negative control; d: T1; e: T2; f: single-base mismatched T1; g: single-base mismatched T2); (E) fluorescence emission spectra for MDR strain, nonresistant strain, and blank; (F) fluorescence emission spectra for RIF-resistant strain, INH-resistant strain, and blank.

Figure 4A, the addition of nanoCoTPyP-2 toward double QDs-ssDNA led to obvious fluorescence intensity decreases of two peaks, indicating the interactions between double QDs-ssDNA and nanoCoTPyP-2. However, due to the presence of two targets, double QDs-ssDNA exhibited significant fluorescence recovery of both peaks, suggesting the hybridization between ssDNA and target DNA. Herein, the fluorescence recovery ratio was assessed by the value of $(F_2 - F_1)/F_0$, where F_0 and F_1 are the fluorescence intensities of QDs-ssDNA without and with nanoCoTPyP, and F_2 is the fluorescence intensity of QDs-ssDNA after the addition of T1 and T2. The fluorescence recovery ratios of these four nanoCoTPyPs for double QDs-ssDNA were calculated (Figure 4B). It could be seen that nanoCoTPyP-1∼nanoCoTPyP-3 had remarkable fluorescence restoring ability for T1 and T2, while nanoCoTPyP-4 could hardly restore the fluorescence. In other words, nanoCoTPyP-1∼nanoCoTPyP-3 could successfully detect T1 and T2 simultaneously, but nanoCoTPyP-4 could not. Among nanoCoTPyP-1, nanoCoTPyP-2, and nanoCoTPyP-3, the detection performance of nanoCoTPyP-2 was slightly better than that of nanoCoTPyP-1 and nanoCoTPyP-3. To confirm the mechanism of DNA detection, nanoCoTPyP-2 was employed to quench the double QDs-ssDNA and double QDs-dsDNA. As illustrated from Figure 4D, when double QDs-ssDNA hybridized with T1 and T2 to form double QDs-dsDNA, the fluorescence quenching efficiency of nanoCoTPyP-2 significantly reduced from 72 to 8%. This demonstrated that the nanoCoTPyP-2 indeed showed obvious adsorption differences towards ssDNA and dsDNA, which enabled the simultaneous determination of T1 and T2. The sensing performance of nanoCoTPyP-4 was further explained. According to the previous study, the negatively charged fluorescence probe could re-adsorb onto the positively charged edge of the MOFs due to electrostatic attractions, which led to the failure of fluorescence restoration.[44] NanoCoTPyP-4 nanosheets were negatively charged, but the edge of the nanoCoTPyP-4 nanosheets contained positively charged pyridine groups. Therefore, we may infer that negatively charged double QDs re-adsorbed onto the positively charged edge of nanoCoTPyP-4 due to electrostatic attractions (Figure 4C). To demonstrate the adhesion of double QDs-dsDNA on nanoCoTPyP-4, the fluorescence intensity of supernatant was detected by centrifuging the mixture of double QDs-dsDNA and nanoCoTPyP-4. After the removal of nanoCoTPyP-4, the fluorescence intensity of supernatant was much lower than that of the pure double QDs-dsDNA (Figure S10). This revealed that the majority of the double QDs-dsDNA was adsorbed on nanoCoTPyP-4 and removed by centrifugation, demonstrating this explanation.

Optimization of Experimental Conditions. Considering the excellent sensing performance of nanoCoTPyP-2 for DNA detection, nanoCoTPyP-2 was selected for the simultaneous

https://doi.org/10.1021/acs.analchem.2c00723
Anal. Chem. 2022, 94, 7918−7927

detection of T1 and T2. To obtain the best quantitative result, several factors, including adsorption time, concentration of nanoCoTPyP-2, and incubation time, were optimized. The adsorption time of double QDs-ssDNA onto nanoCoTPyP-2 was firstly optimized. As presented in Figure S11A,B, the fluorescence intensity of both peaks gradually decreased and stabilized at 4 min. Therefore, 4 min was selected as the efficient time for the adhesion of double QDs-ssDNA and nanoCoTPyP-2. Additionally, the insufficient and excessive amounts of nanoCoTPyP-2 were not conducive to target DNA detection. Therefore, the concentration of nanoCoTPyP-2 was further optimized. It was observed that the maximum fluorescence recovery ratio occurred at the concentration of 4.0 μM (Figure S11C). Thus, the best concentration of nanoCoTPyP-2 was considered as 4.0 μM for subsequent detection. The incubation time for T1 and T2 detection was finally investigated. The fluorescence intensities of the two peaks reached a plateau at 6 min for QDs1-ssDNA1 and at 7 min for QDs2-ssDNA2 (Figure S11D). Therefore, 7 min was chosen as the incubation time for T1 and T2 detection.

Simultaneous Detection of Multiple DNA. Under optimal conditions, the simultaneous detections of T1 and T2 were performed using double QDs-ssDNA and nanoCoTPyP-2. As shown in Figure 5A, the fluorescence intensities at 535 and 648 nm were gradually increased with the increasing concentrations of T1 (0.04 nM-27 nM) and T2 (0.03−25 nM). The fluorescence intensities of the two peaks at 535 and 648 nm displayed a good linear response to the concentrations of T1 and T2 (Figure 5B,C). The linear regression equation for T1 is given by $Y = 10.6773X + 189.8815$ in the range of 0.04−27 nM. Another linear equation for T2 fitted as $Y = 11.8166X + 245.6869$ in the range from 0.03 to 25 nM. The R^2 values of T1 and T2 were 0.9974 and 0.9995, respectively. The limits of detection (LODs) for T1 and T2 were calculated as 24 and 20 pM, based on the definition of the ratio of three times the deviation of blank signal to the slope. Compared with other nanomaterial-based fluorescence biosensors for nucleic acid detection without signal amplification, our strategies exhibited low LODs along with multiplexed detection and simple operation (Table S4). The relative standard deviations (RSDs) of the intra-assays and inter-assays for T1 and T2 were not more than 3.3% (Table S5), indicating that the fluorescence sensing platform was equipped with good precision and reproducibility. Moreover, the selectivity of our proposed method was further studied by using interferents including single-base mismatched T1, single-base mismatched T2, and completely base mismatched DNA as negative control (Figure 5D), revealing the great specificity of our methods.

Application in Clinical MDR Strains. Furthermore, to demonstrate the ability to distinguish drug-resistant genes in real samples, this fluorescence biosensor was utilized to detect the clinical tuberculosis pathogen. Twenty strain samples, including five MDR strains, seven nonresistant strains (called S), three RIF-resistant strains, and five INH-resistant strains, were amplified by PCR, and then tested by our methods. As shown in Figures 5E and S12, MDR strains could significantly recovery the fluorescence signals at both 537 and 648 nm, while nonresistant strains barely changed the fluorescence intensity of the two peaks, demonstrating excellent ability for real-sample analysis. Additionally, this approach could also successfully discriminate the single-resistant strains (Figures 5F and S12). The concentrations of PCR products of RIF- and INH-resistant genes were determined based on gel electrophoresis and gray value measurement (Figure S13), and their final concentrations were acceptable for the detection. The detection methods, including PCR and fluorescence analysis, could be completed within 95 min, showing a great potential for rapid screening of MDR-TB.

CONCLUSIONS

In summary, a novel one-step fluorescence sensing platform was developed for simultaneous detection of Mtb multidrug-resistant genes (rpoB531 and katG315) based on nanoCoTPyP-2 and double QDs-ssDNA probes. NanoCoTPyP-based 2D and 3D nanomaterials were successfully prepared through the surfactant-assisted synthesis method, and the effect of surface charge property and geometry structure on the sensing performance was discussed in detail. We demonstrated that multidrug-resistant genes could be successfully quantified by measuring the fluorescence emission spectra in a single run. Compared with the reported nanomaterial-based biosensors, our approach illustrated better comprehensive performance in simultaneously detecting multiple DNAs. It is worth mentioning that this proposed strategy could achieve the simultaneous detection of two mutant genes in clinical PCR products of MDR-TB. Our fluorescence method combined with PCR only takes 95 min in total. This approach with remarkable advantages, including high sensitivity, time saving, and low cost, may open a new avenue to clinical application, including drug resistance diagnosis and clinical drug guidance.

ASSOCIATED CONTENT

Supporting Information

The Supporting Information is available free of charge at https://pubs.acs.org/doi/10.1021/acs.analchem.2c00723.

Detail experimental procedures; nucleotide sequences of DNA (Table S1), clinical strain information (Table S2), K_{sv} results (Table S3); comparison with other literatures (Table S4), intra-/inter-assay results (Table S5); FRET process (Figure S1); XPS spectra and AFM image (Figure S2); DLS distribution (Figure S3); UV−vis spectra and fluorescence spectra (Figure S4); DNA loading on QDs (Figure S5); quenching behaviors of nanoCoTPyP (Figure S6); maximum quenching efficiency (Figure S7); quenching efficiency of Co^{2+}, TPyP, CoTPyP and nanoCoTPyP (Figure S8); characterizations of nanoCoTPyP-5 and nanoCoTPyP-6 (Figure S9); inefficiency of nanoCoTPyP-4 (Figure S10); optimization of experimental conditions (Figure S11); detection of real samples (Figure S12); gel electroanalysis (Figure S13) (PDF)

AUTHOR INFORMATION

Corresponding Authors

Yanli Tong − *Guangdong Second Provincial General Hospital, Guangzhou 510317, P. R. China*; Email: tongh2008@126.com

Yaoju Tan − *State Key Laboratory of Respiratory Disease, Department of Clinical Laboratory, Guangzhou Chest Hospital, Guangzhou 510095, P. R. China*; Email: gzchtan@163.com

Zuanguang Chen − *School of Pharmaceutical Sciences, Sun Yat-sen University, Guangzhou 510006, P. R. China*; orcid.org/0000-0002-3273-3829; Phone: +86-20-

https://doi.org/10.1021/acs.analchem.2c00723
Anal. Chem. 2022, 94, 7918−7927

39943044; Email: chenzg@mail.sysu.edu.cn; Fax: +86-20-39943071

Authors

Ou Hu − *School of Pharmaceutical Sciences, Sun Yat-sen University, Guangzhou 510006, P. R. China*

Zeyu Li − *School of Pharmaceutical Sciences, Sun Yat-sen University, Guangzhou 510006, P. R. China*

Qidi He − *School of Pharmaceutical Sciences, Sun Yat-sen University, Guangzhou 510006, P. R. China*

Complete contact information is available at: https://pubs.acs.org/10.1021/acs.analchem.2c00723

Author Contributions

O.H. performed the experiments and data analysis and wrote the manuscript. Z.L. conducted the PCR experiments of the clinical samples. Q.H. helped with the data analysis. Y.T. collected and treated the clinical strain samples. Y.T. and Z.C. secured funding and contributed to the experimental design. All of the authors reviewed and approved the manuscript.

Notes

The authors declare no competing financial interest.

■ ACKNOWLEDGMENTS

The authors are grateful to the financial support from the Science and Technology Planning Project of Guangzhou (No. 202002020084), the Project of Guangdong Administration of Traditional Chinese Medicine (No. 20191014), and the National Natural Science Foundation of China (No. 21675177).

■ REFERENCES

(1) Russell, D. G.; Cardona, P. J.; Kim, M. J.; Allain, S.; Altare, F. *Nat. Immunol.* **2009**, *10*, 943−948.
(2) Miyata, M.; Pavan, F. R.; Sato, D. N.; Marino, L. B.; Hirata, M. H.; Cardoso, R. F.; de Melo, F. A. F.; Zanelli, C. F.; Leite, C. Q. F. *Biomed. Pharmacother.* **2011**, *65*, 456−459.
(3) Bang, H.; Park, S.; Hwang, J.; Jin, H.; Cho, E.; Kim, D. Y.; Song, T.; Shamputa, I. C.; Via, L. E.; Barry, C. E.; Cho, S. N.; Lee, H. *J. Med. Microbiol.* **2011**, *60*, 1447−1454.
(4) Abate, G.; Hoffner, S. E.; Thomsen, V. O.; Miorner, H. *Eur. J. Clin. Microbiol. Infect. Dis.* **2001**, *20*, 329−333.
(5) Dorman, S. E.; Schumacher, S. G.; Alland, D.; et al. *Lancet Infect. Dis.* **2018**, *18*, 76−84.
(6) Li, Q. J.; Jiao, W. W.; Yin, Q. Q.; Li, Y. J.; Li, J. Q.; Xu, F.; Sun, L.; Xiao, J.; Qi, H.; Wang, T.; Mokrousov, I.; Huang, H. R.; Shen, A. D. *Int. J. Antimicrob. Agents* **2017**, *49*, 757−762.
(7) Ahmad, S.; Mokaddas, E. *Int. J. Antimicrob. Agents* **2004**, *23*, 473−479.
(8) Lawn, S. D.; Mwaba, P.; Bates, M.; Piatek, A.; Alexander, H.; Marais, B. J.; Cuevas, L. E.; McHugh, T. D.; Zijenah, L.; Kapata, N.; Abubakar, I.; McNerney, R.; Hoelscher, M.; Memish, Z. A.; Migliori, G. B.; Kim, P.; Maeurer, M.; Schito, M.; Zumla, A. *Lancet Infect. Dis.* **2013**, *13*, 349−361.
(9) Ibrahim, S. A.; Chan, Y. *ACS Appl. Mater. Interfaces* **2021**, *13*, 35294−35305.
(10) Chang, F.; Huang, L. J.; Guo, C. Z.; Xie, G. M.; Li, J. Q.; Diao, Q. Z. *ACS Appl. Mater. Interfaces* **2019**, *11*, 35622−35629.
(11) Luo, L. H.; Zhang, F.; Chen, C. Y.; Cai, C. Q. *Anal. Chem.* **2019**, *91*, 15748−15756.
(12) Li, L. Y.; Li, Q. J.; Liao, Z. Y.; Sun, Y.; Cheng, Q. S.; Song, Y.; Song, E. Q.; Tan, W. H. *Anal. Chem.* **2018**, *90*, 9621−9628.
(13) Xie, K. X.; Liu, Q.; Song, X. L.; Huo, R. P.; Shi, X. H.; Liu, Q. L. *Anal. Chem.* **2021**, *93*, 3671−3676.
(14) Wu, M.; Chen, Z. K.; Xie, Q. H.; Xiao, B. L.; Zhou, G.; Chen, G.; Bian, Z. *Biosens. Bioelectron.* **2021**, *171*, No. 112733.
(15) Goryacheva, O. A.; Guhrenz, C.; Schneider, K.; Beloglazova, N. V.; Goryacheva, I. Y.; De Saeger, S.; Gaponik, N. *ACS Appl. Mater. Interfaces* **2020**, *12*, 24575−24584.
(16) Ouyang, Y.; Zhang, P.; Manis-Levy, H.; Paltiel, Y.; Willner, I. *J. Am. Chem. Soc.* **2021**, *143*, 17622−17632.
(17) Wang, J. J.; Zheng, C. S.; Jiang, Y. Z.; Zheng, Z. H.; Lin, M.; Lin, Y.; Zhang, Z. L.; Wang, H. Z.; Pang, D. W. *Anal. Chem.* **2020**, *92*, 830−837.
(18) Wu, S. J.; Ren, D. M.; Zhou, K.; Xia, H. L.; Liu, X. Y.; Wang, X. T.; Li, J. *J. Am. Chem. Soc.* **2021**, *143*, 10547−10552.
(19) Yang, L. T.; Cai, P. Y.; Zhang, L. L.; Xu, X. Y.; Yakovenko, A. A.; Wang, Q.; Pang, J. D.; Yuan, S.; Zou, X. D.; Huang, N.; Huang, Z. H.; Zhou, H. C. *J. Am. Chem. Soc.* **2021**, *143*, 12129−12137.
(20) Wu, M. X.; Wang, Y.; Zhou, G. H.; Liu, X. M. *ACS Appl. Mater. Interfaces* **2020**, *12*, 54285−54305.
(21) Lv, M. Z.; Zhou, W.; Tavakoli, H.; Bautista, C.; Xia, J. F.; Wang, Z. H.; Li, X. J. *Biosens. Bioelectron.* **2021**, *176*, No. 112947.
(22) Wang, H. S.; Liu, H. L.; Wang, K.; Ding, Y.; Xu, J. J.; Xia, X. H.; Chen, H. Y. *Anal. Chem.* **2017**, *89*, 11366−11371.
(23) Zhang, H. T.; Zhang, J. W.; Huang, G.; Du, Z. Y.; Jiang, H. L. *Chem. Commun.* **2014**, *50*, 12069−12072.
(24) Hao, Y. B.; Shao, Z. S.; Cheng, C.; Xie, X. Y.; Zhang, J.; Song, W. J.; Wang, H. S. *ACS Appl. Mater. Interfaces* **2019**, *11*, 31755−31762.
(25) Xie, X. Y.; Ke, R. F.; Cheng, C.; Wang, Y. H.; Song, Z.; Zhang, C. D.; Wang, H. S. *Biosens. Bioelectron.* **2021**, *176*, No. 112896.
(26) Yang, S. P.; Zhao, W.; Hu, P. P.; Wu, K. Y.; Jiang, Z. H.; Bai, L. P.; Li, M. M.; Chen, J. X. *Inorg. Chem.* **2017**, *56*, 14880−14887.
(27) He, X. H.; He, Q.; Deng, Y. C.; Peng, M.; Chen, H. Y.; Zhang, Y.; Yao, S. Y.; Zhang, M. T.; Xiao, D. Q.; Ma, D.; Ge, B. H.; Ji, H. B. *Nat. Commun.* **2019**, *10*, No. 3633.
(28) Fry, H. C.; Garcia, J. M.; Medina, M. J.; Ricoy, U. M.; Gosztola, D. J.; Nikiforov, M. P.; Palmer, L. C.; Stupp, S. I. *J. Am. Chem. Soc.* **2012**, *134*, 14646−14649.
(29) Qiu, Y. F.; Chen, P. L.; Liu, M. H. *J. Am. Chem. Soc.* **2010**, *132*, 9644−9652.
(30) Wang, Y.; Hu, Y. Q.; He, Q. Y.; Yan, J. H.; Xiong, H. J.; Wen, N. C.; Cai, S. D.; Peng, D. M.; Liu, Y. F.; Liu, Z. B. *Biosens. Bioelectron.* **2020**, *169*, No. 112604.
(31) Ennassiri, W.; Jaouhari, S.; Sabouni, R.; Cherki, W.; Charof, R.; Filali-Maltouf, A.; Lahlou, O. *J. Global Antimicrob. Resist.* **2018**, *12*, 197−201.
(32) Zhao, M. T.; Wang, Y. X.; Ma, Q. L.; Huang, Y.; Zhang, X.; Ping, J. F.; Zhang, Z. C.; Lu, Q. P.; Yu, Y. F.; Xu, H.; Zhao, Y. L.; Zhang, H. *Adv. Mater.* **2015**, *27*, 7372−7378.
(33) Fu, H. Y.; Hu, O.; Fan, Y.; Hu, Y.; Huang, J. H.; Wang, Z.; She, Y. B. *Sens. Actuators, B* **2019**, *287*, 1−8.
(34) Sławski, J.; Bialek, R.; Burdzinski, G.; Gibasiewicz, K.; Worch, R.; Grzyb, J. *J. Phys. Chem. B* **2021**, *125*, 3307−3320.
(35) Van Galen, D. A.; Majda, M. *Anal. Chem.* **1988**, *60*, 1549−1553.
(36) Hu, O.; Li, Z. Y.; Tong, Y. L.; Wang, Q. Y.; Chen, Z. G. *Talanta* **2021**, *235*, No. 122763.
(37) de Sousa Neto, D.; Hawe, A.; Tabak, M. *Eur. Biophys. J.* **2013**, *42*, 267−279.
(38) Fukui, T.; Kawai, S.; Fujinuma, S.; Matsushita, Y.; Yasuda, T.; Sakurai, T.; Seki, S.; Takeuchi, M.; Sugiyasu, K. *Nat. Chem.* **2017**, *9*, 493−499.
(39) Deng, S. Y.; Yuan, P. X.; Ji, X. B.; Shan, D.; Zhang, X. J. *ACS Appl. Mater. Interfaces* **2015**, *7*, 543−552.
(40) Hinoue, T.; Kobayashi, J.; Ozeki, T.; Watarai, H. *Chem. Lett.* **1997**, *26*, 763−764.
(41) Zhong, Y.; Wang, J. F.; Zhang, R. F.; Wei, W. B.; Wang, H. M.; Lu, X. P.; Bai, F.; Wu, H. M.; Haddad, R.; Fan, H. Y. *Nano Lett.* **2014**, *14*, 7175−7179.

(42) Zhao, H. Q.; Qiu, G. H.; Liang, Z.; Li, M. M.; Sun, B.; Qin, L.; Yang, S. P.; Chen, W. H.; Chen, J. X. *Anal. Chim. Acta* **2016**, *922*, 55−63.
(43) Ding, L. P.; Wang, S. H.; Liu, Y.; Cao, J. H.; Fang, Y. *J. Mater. Chem. A* **2013**, *1*, 8866−8875.
(44) Wang, H. S.; Li, J.; Li, J. Y.; Wang, K.; Ding, Y.; Xia, X. H. *NPG Asia Mater.* **2017**, *9*, No. e354.

https://doi.org/10.1021/acs.analchem.2c00723
Anal. Chem. 2022, 94, 7918−7927